

# Himawari-8-derived diurnal variations of ground-level PM<sub>2.5</sub> pollution across China using the fast space-time Light Gradient Boosting Machine

5 Jing Wei<sup>1, 2, 3\*</sup>, Zhanqing Li<sup>2\*\*</sup>, Rachel T. Pinker<sup>2</sup>, Jun Wang<sup>3</sup>, Lin Sun<sup>4</sup>, Wenhao Xue<sup>1</sup>, Runze Li<sup>1</sup>,  
Maureen Cribb<sup>2</sup>

1. State Key Laboratory of Remote Sensing Science, College of Global Change and Earth System Science, Beijing Normal University, Beijing, China
- 10 2. Earth System Science Interdisciplinary Center, Department of Atmospheric and Oceanic Science, University of Maryland, College Park, MD, USA
3. Department of Chemical and Biochemical Engineering, Iowa Technology Institute, The University of Iowa, Iowa City, IA, USA
4. College of Geodesy and Geomatics, Shandong University of Science and Technology, Qingdao, China

15

Correspondence to: Jing Wei (weijing\_rs@163.com), Zhanqing Li (zli@atmos.umd.edu)

## Abstract

20 Information on the particulate matter with a diameter of less than 2.5  $\mu\text{m}$  (PM<sub>2.5</sub>) has been used as an important atmospheric environmental parameter mainly because of its impact on human health. PM<sub>2.5</sub> is affected by both natural and anthropogenic factors that usually have strong diurnal variations. Such information helps toward understanding the causes of air pollution as well as our adaptation to it. Most existing PM<sub>2.5</sub> products have been derived from polar-orbiting satellites. This study exploits the use of  
25 the next-generation geostationary meteorological satellite Himawari-8/AHI to document the diurnal variation of PM<sub>2.5</sub>. Given the huge volume of satellite data, based on the idea of gradient boosting, a highly efficient tree-based Light Gradient Boosting Machine (LightGBM) method by involving the spatiotemporal characteristics of air pollution, namely the space-time LightGBM (STLG) model, is developed. An hourly PM<sub>2.5</sub> dataset for China (ChinaHighPM<sub>2.5</sub>) at a 5-km spatial resolution is derived

30 based on Himawari-8/AHI aerosol products with additional environmental variables. Hourly PM<sub>2.5</sub> estimates (number of data samples = 1,415,188) are well correlated with ground measurements in China (cross-validation coefficient of determination, CV-R<sup>2</sup> = 0.85), with a root-mean-square error (RMSE) and mean absolute error (MAE) of 13.62 and 8.49  $\mu\text{g}/\text{m}^3$ , respectively. Our model captures well the PM<sub>2.5</sub> diurnal variations showing that pollution increases gradually in the morning, reaching a peak at  
35 about 10:00 a.m. local time, then decreases steadily until sunset. The proposed approach outperforms most traditional statistical regression and tree-based machine-learning models, with a much lower computation burden in terms of speed and memory, making it most suitable for routine pollution monitoring.

## 40 1. Introduction

China has faced severe environmental problems during the last two decades, especially air pollution (An et al., 2019; Chan & Yao, 2008; Z. Li et al., 2017; Q. Zhang et al., 2019). The sources of air pollution are numerous, coming from both natural changes (e.g., forest fires, biomass burning) and human activities (e.g., industrial production, transportation) (Huang et al., 2014; Sun et al., 2004; Wei et al.,  
45 2019a). Particulate matter with a diameter of less than 2.5  $\mu\text{m}$  (PM<sub>2.5</sub>) has a greater impact on the atmospheric environment and climate change than other air pollutants [e.g., PM<sub>10</sub>, nitrogen dioxide (NO<sub>2</sub>), and sulfur dioxide (SO<sub>2</sub>)] (Jacob & Winner, 2009; Z. Li et al., 2017, 2019; Ramanathan & Feng, 2009). Moreover, they can cause great harm to human health due to their smaller particle size (Delfino et al., 2005; Kampa & Castanas, 2008; Kim et al., 2015; Lelieveld et al., 2015). China has established  
50 and operates multiple ground-based observation networks to monitor air pollution in real-time across mainland China, including information about PM<sub>2.5</sub> pollution.

For near-surface concentrations, the networks provide high-quality PM<sub>2.5</sub> measurements every hour (even every few minutes) but with non-uniform coverage. In recent years, an increased effort has been made in estimating PM<sub>2.5</sub> with products generated from multiple instruments on sun-synchronous  
55 satellites, e.g., the Multi-angle Imaging SpectroRadiometer (MISR) (Y. Liu et al., 2005; van Donkelaar et al., 2006), the Moderate-resolution Imaging Spectroradiometer (MODIS) (Y. Liu et al., 2007; Ma et al., 2014; Wei et al., 2019a, 2020, 2021a), and the Visible infrared Imaging Radiometer (VIIRS) (Wei et

al., 2021b; Wu et al., 2016; Yao et al., 2019). However, due to their low revisit cycles (one or two overpasses per day), they are unable to monitor the diurnal variation of pollution. Currently, most 60 available PM<sub>2.5</sub> datasets are at low temporal resolutions that cannot meet the requirements of air pollution real-time monitoring (Lennartson et al., 2018). For example, knowing when heavy pollution might occur during the day, people may adjust their time outdoors doing activities accordingly. Following the launch of the Himawari-8/Advanced Himawari Imager (AHI) on 7 October 2014 (Bessho et al., 2016; Letu et al., 2020), near-surface PM<sub>2.5</sub> concentrations in the Eastern Hemisphere can now be 65 estimated and used to examine their diurnal cycle.

W. Wang et al. (2017) used the linear mixed-effect (LME) model, and Sun et al. (2019) applied the geographically weighted regression (GWR) and support vector regression (SVR) models to estimate hourly PM<sub>2.5</sub> concentrations in the Beijing–Tianjin–Hebei (BTH) region from the Himawari-8 aerosol optical depth (AOD) product. T. Zhang et al. (2019) developed an improved LME model, and Xue et al. 70 (2020) proposed an improved geographically and temporally weighted regression (IGTWR) model to derive hourly PM<sub>2.5</sub> maps based on the Himawari-8 AOD product over central and eastern China. In addition to traditional statistical regression models, several artificial intelligence models, including the random forest (RF), the gradient boosting decision tree (GBDT), the eXtreme Gradient Boosting (XGBoost), and the deep neural network (DNN), have been recently successfully adopted to obtain 75 ground-level PM<sub>2.5</sub> concentrations to local regions and to the whole of China (J. Chen et al., 2019; Gui et al., 2020; J. Liu et al., 2019; Sun et al., 2019; T. Zhang et al., 2020). Nevertheless, due to their poor data-mining ability, traditional statistical regression methods usually suffer from large uncertainties. While artificial intelligence methods can achieve high accuracies, they are often highly demanding on 80 computational power and are thus often slow. Therefore, Spatiotemporal variations of PM<sub>2.5</sub> have often been neglected in the models developed in previous studies (J. Chen et al., 2019; J. Liu et al., 2019; Sun et al., 2019; W. Wang et al., 2017; T. Zhang et al., 2019), resulting in relatively low accuracies. Focusing on the above issues, we have developed a new, highly efficient, and precise method for 85 improving ground-level PM<sub>2.5</sub> estimates by incorporating spatial and temporal information into the tree-based Light Gradient Boosting Machine (LightGBM) model. This new model is called the space-time LightGBM (STLG) model, used to generate a high-quality, high-temporal-resolution (hourly) PM<sub>2.5</sub>

dataset over eastern China (at a spatial resolution of 5 km) from the Himawari-8/AHI hourly AOD product. Section 2 provides details about the data used and introduces the development of the STLG model. Section 3 validates the hourly PM<sub>2.5</sub> estimates and shows the diurnal PM<sub>2.5</sub> variations across China. Comparisons with results from traditional models and from previous studies are also presented.

90 Section 4 summarizes the study.

## 2. Materials and methods

### 2.1 Data sources

#### 2.1.1 PM<sub>2.5</sub> and AOD data

95 PM<sub>2.5</sub> hourly measurements from 1583 monitoring stations across China for the year 2018 were collected [Figure 1 in Wei et al. (2020)]. The latest Himawari-8 Version 2 hourly 5-km AODs at 500 nm across mainland China for that year were also collected. This AOD product is synthesized from Level 2 10-minute AODs, generated by a newly developed Lambertian-surface-assumed aerosol retrieval algorithm (Letu et al., 2018; Yoshida et al., 2018). Himawari-8 AOD retrievals have been 100 preliminarily evaluated against in situ AOD retrievals provided by the Aerosol Robotic Network (Giles et al., 2019) and the Sun–Sky Radiometer Observation Network (Z. Li et al., 2018), showing that they are consistent ( $R = 0.75$ ), with a root-mean-square error (RMSE) and mean absolute error (MAE) of 0.39 and 0.21, respectively (Wei et al., 2019b). Here, only low-uncertainty AOD retrievals (500 nm) were selected for estimating PM<sub>2.5</sub> concentrations.

105

#### 2.1.2 Meteorological conditions

PM<sub>2.5</sub> can be significantly affected by meteorological conditions (Su et al., 2018). However, most currently available reanalysis meteorological products have low temporal resolutions (~3–6 hours). Recently (14 June 2018), the fifth-generation European Centre for Medium-range Weather Forecasts 110 (ECMWF) global atmospheric reanalysis (ERA5) at a horizontal resolution of  $0.25^\circ \times 0.25^\circ$  has been released, as well as the land version (12 July 2019) at a horizontal resolution of  $0.1^\circ \times 0.1^\circ$ , both at an hourly time scale (1979 to the present). Here, we use seven ERA5 hourly meteorological parameters,

i.e., the 2-m temperature (TEM), total evaporation (ET), relative humidity (RH), 10-m u- and v-components of wind, surface pressure (SP), and boundary-layer height (BLH).

115

### 2.1.3 Human influences

Human activity is a key factor affecting PM<sub>2.5</sub> pollution. The global annual LandScan<sup>TM</sup> product at a 1-km spatial resolution for the year 2018 was selected to obtain the population distribution (POP) (Dobson et al., 2000). Monthly anthropogenic source emission data from the Multi-resolution Emission 120 Inventory for China (MEIC) (M. Li et al., 2017; Zheng et al., 2018) were also employed. This dataset is generated from agricultural, industrial, power, residential, and transportation information obtained at more than 700 anthropogenic sources, including a total of 10 atmospheric pollutants and greenhouse gases. Here, four main precursors were selected, i.e., ammonia (NH<sub>3</sub>), nitrogen oxides (NO<sub>x</sub>), SO<sub>2</sub>, and volatile organic compounds (VOC), and direct emissions to PM.

125

### 2.1.4 Ancillary data

Two additional ancillary datasets, namely, the MODIS monthly Normalized Difference Vegetation Index (NDVI) at a horizontal resolution of  $0.05^{\circ} \times 0.05^{\circ}$  and the Shuttle Radar Topography Mission (SRTM) 90-m digital elevation model (DEM) products, were selected to characterize land cover, its 130 change and topographical conditions in China. All selected variables (Table 1) with potential impacts on PM<sub>2.5</sub> concentrations were resampled to the same spatial resolution as the Himawari-8 aerosol product, namely,  $0.05^{\circ} \times 0.05^{\circ}$ .

*[Please insert Table 1 here]*

## 2.2 Space-Time LightGBM model

### 135 2.2.1 LightGBM model

The LightGBM model, a newly developed tree-based machine-learning approach, was introduced in 2017 (Ke et al., 2017). Using the gradient boosting framework to construct the decision tree, this approach can tackle both regression and classification tasks, and as such can be expanded for PM

applications. It can also tackle the main challenge faced in traditional machine-learning approaches  
140 namely, computational complexities, which are very time-consuming. LightGBM is a fast, distributed, and highly efficient method that reduces the number of data samples ( $M$ ) and features ( $N$ ). The LightGBM model includes three main steps when constructing the decision tree:

- 1) Histogram-based algorithm. Continuous features are first converted to different bins, which are used to construct feature index histograms without the need to sort during training. It goes through all the data bins to find the best split point from the feature histograms, which can significantly reduce the computation cost of the split gain. The overall complexity is  $O(M \times N)$ .
- 2) Gradient-based one-side sampling. Data samples are first sorted in descending order according to their absolute gradients, and the top  $a\%$  of them are selected as a subset sample with large gradients. The  $b\%$  samples are then randomly chosen from the remaining data as a subset sample with small gradients. The sampled data with small gradients are multiplied by a weight coefficient,  $(\frac{1-a}{b})$ . Consequently, a new classifier is learned and established using the above-sampled data until convergence.
- 3) Exclusive feature bundling. A graph with weighted edges is first constructed, and each weight corresponds to the total number of conflicts between two features. The features are then sorted in descending order according to the degree of each feature (the greater the degree, the greater the conflict with other points). Last, each feature is checked in the sorted sequence and either assigned to a combination with small conflicts or created a new combination.

In addition to the main technologies mentioned above, there are other features of the optimization, such as the leaf-wise tree growth strategy with depth restriction (Shi, 2007), histogram difference

160 acceleration, sequential access gradient, and the support of category feature and parallel learning. These advanced methodologies make it possible to reach a high accuracy and efficiency (Ke et al., 2017).

### 2.2.2 Model development

It is well known that air pollution has spatiotemporal heterogeneity, leading to large differences in  
165 PM<sub>2.5</sub> concentrations in both time and space. Such characteristics have always been ignored in most traditional statistical regression and artificial intelligence methods. Studies have shown that including

spatiotemporal information has led to improved PM<sub>2.5</sub> estimates using remote sensing techniques (Z. Li et al., 2017; Wei et al., 2019a, 2020). Therefore, we have introduced a new approach to 170 integrates spatiotemporal information into the LightGBM model. The new model developed here is called the STLG model. The spatial feature is represented by the geographical distances of one pixel to other points in the circumscribed rectangle of the study region (Baez-Villanueva et al., 2020; Behrens et al., 2018). The distance is calculated using the haversine method (Equation 1) to reflect the spherical 175 distance between two points in the sphere space (Wei et al., 2021a). The temporal feature is represented by the day of the year (DOY), used to distinguish each data record on different days of the year during the model training.

$$DIS = 2 * r * \arcsin \left( \sqrt{\sin^2 \left( \frac{\varphi_2 - \varphi_1}{2} \right) + \cos(\varphi_1) \cos(\varphi_2) \sin^2 \left( \frac{\gamma_2 - \gamma_1}{2} \right)} \right), \quad (1)$$

where  $\varphi$  and  $\gamma$  represent the latitude and longitude of a point on the sphere, respectively, and  $r$  denotes Earth's mean radius ( $\approx 6371$  km). Figure 1 illustrates the flowchart of the new STLG model.

*[Please insert Figure 1 here]*

180 In addition to Himawari-8 AODs, other auxiliary variables were considered and employed to improve PM<sub>2.5</sub>-AOD relationships. However, to avoid redundant information, we first calculated the normalized importance (%) of each feature to the PM<sub>2.5</sub> estimation during the model training (Figure 2). It represents the total gains of splits that use the feature during the decision-tree construction, but not the physical contribution. AOD is found to be the most important feature, accounting for about 17%. All 185 meteorological factors have an important impact on the PM<sub>2.5</sub> estimation, especially BLH, RH, and TEM (importance  $> 8\%$ ) followed by two surface-related variables (i.e., NDVI and DEM) and POP. The influence of aerosol precursors and emissions (i.e., NH<sub>3</sub>, NO<sub>x</sub>, SO<sub>2</sub>, PM, and VOC) on the PM<sub>2.5</sub> estimation cannot be ignored (importance  $> 2\%$ ). Therefore, all 16 selected variables are included to establish the final model in this study.

190 *[Please insert Figure 2 here]*

Here, two independent ten-fold cross-validation methods (10-CV) (Rodriguez et al., 2010), based on all the data samples (i.e., out-of-sample) and PM<sub>2.5</sub> monitoring stations (i.e., out-of-station), were selected to validate the model performance and the spatial prediction ability, respectively.

195 **3. Results and discussion**

**3.1 Model fitting and validation**

**3.1.1 Spatial-scale performance**

The STLG model can largely minimize overfitting, showing a strong data-mining ability (Figure 3), which can more accurately establish the relationships between hourly PM<sub>2.5</sub> observations and influential variables (i.e., coefficient of determination,  $R^2 = 0.97\text{--}0.98$ , RMSE = 4.18–7.31  $\mu\text{g}/\text{m}^3$ ). Figure 4 illustrates the out-of-sample evaluation results of estimated hourly PM<sub>2.5</sub> values over China from 08:00 to 17:00 local time in 2018. The STLG model is highly accurate in estimating hourly PM<sub>2.5</sub> concentrations, with high sample-based CV- $R^2$  values ranging from 0.81 to 0.85, strong slopes of ~0.81–0.84, and small y-intercepts of ~5.52–7.84  $\mu\text{g}/\text{m}^3$ . The uncertainties are overall small, with RMSEs (MAEs) ranging from 11.24 (6.82)  $\mu\text{g}/\text{m}^3$  to 15.56 (9.79)  $\mu\text{g}/\text{m}^3$ . However, the STLG performs slightly differently, with small differences in main evaluation indicators throughout the day. The main reasons being that the number of training samples is reduced during sunrise (Figure 4a-b) and sunset (Figure 4i-j) in optical remote sensing, affecting the model training. Air pollution also has clear diurnal variations at different PM<sub>2.5</sub> pollution levels due to the different intensities of human activities and natural conditions. In general, our model is stable and robust, with an equal out-of-sample CV- $R^2$  of 0.85 and an equal regression slope of 0.81 at most hours during the day in China (Figure 4c-h).

*[Please insert Figures 3 and 4 here]*

Furthermore, out-of-station CV- $R^2$  values range from 0.76 to 0.81, and RMSE (MAE) values range from 12.49 (7.85)  $\mu\text{g}/\text{m}^3$  to 17.61 (11.33)  $\mu\text{g}/\text{m}^3$  (Figure 5), indicating that our model has a strong spatial prediction ability and can well predict PM<sub>2.5</sub> values in those areas without surface observations.. The station-based accuracy is also slightly decreased with reference to the sample-based accuracy,

220 further illustrating the robustness of our model. However, two cross-validation results (e.g., slopes = 0.78–0.84) indicate that hourly PM<sub>2.5</sub> concentrations are overall underestimated (Figures 4–5), a common issue in fine-particle remote sensing (Wei et al., 2020). This can be explained by the large aerosol retrieval uncertainty, as well as the small number of data samples under highly polluted conditions (Wei et al., 2019b, c).

*[Please insert Figure 5 here]*

225 Evaluated was also the regional performance of the STLG model for hourly PM<sub>2.5</sub> estimates (Figure 6). Hourly PM<sub>2.5</sub> estimates (number of data samples,  $N = 1,151,595$ ) are highly consistent with ground measurements, with a high sample-based CV-R<sup>2</sup> of 0.87 and a strong regression slope of 0.86, showing small estimation uncertainties (i.e., RMSE = 12.77  $\mu\text{g}/\text{m}^3$ , MAE = 8.12  $\mu\text{g}/\text{m}^3$ ) over Eastern China. The STLG model performs well (e.g., CV-R<sup>2</sup> = 0.88, slope = 0.87) in two typical urban agglomerations of public concern in China, i.e., the Beijing-Tianjin-Hebei (BTH) (Figure 6b) and Yangtze River Delta (YRD) (Figure 6c) regions. By contrast, our model performs relatively poorly in the Pearl River Delta (PRD) region (Figure 6d), possibly due to the significant reduction in the number of data samples caused by frequent, long-term cloud cover in southern China. Note that there are some differences in the uncertainty of hourly PM<sub>2.5</sub> estimates mainly because of varying levels of air pollution. The pollution level in the BTH region is about three times higher than that in the PRD region.

*[Please insert Figure 6 here]*

235 Figure 7 shows the accuracy of the STLG model at each monitoring station across China. At the individual-site scale, the number of data samples gradually decreases from northern China to southern China, mainly due to increasing cloud contamination, with a site average of 997 data samples in China. Except for several scattered monitoring stations in western China, the STLG model has a high performance and adaptability and can well estimate hourly PM<sub>2.5</sub> concentrations at most monitoring 240 stations (e.g., average CV-R<sup>2</sup> = 0.78, RMSE = 12.21  $\mu\text{g}/\text{m}^3$ , and MAE = 8.17  $\mu\text{g}/\text{m}^3$ ). In general, approximately 76%, 79%, and 82% of monitoring stations show high accuracy, with out-of-sample CV-

$R^2$  values  $> 0.7$ , RMSE values  $< 15 \mu\text{g}/\text{m}^3$ , and MAE values  $< 10 \mu\text{g}/\text{m}^3$  in hourly PM<sub>2.5</sub> estimates, especially for those located in central and northern China.

*[Please insert Figure 7 here]*

245 **3.1.2 Temporal-scale performance**

We first quantified the time series of the bias in hourly PM<sub>2.5</sub> estimates during the day in China (Figure 8). There is a slight temporal dependence, where the PM<sub>2.5</sub> bias increases gradually with increasing standard deviation, reaching a maximum around 11:00 a.m., and subsequently decreasing. This seems to be closely related to the diurnal variation of PM<sub>2.5</sub> concentrations. The PM<sub>2.5</sub> estimates are less affected 250 by the time-dependent bias in the Himawari-8 AOD product (Wei et al., 2019b) because machine learning is not sensitive to the systematic bias of aerosol retrievals (Wei et al., 2021b). Nevertheless, our model is generally robust, and can accurately estimate PM<sub>2.5</sub> concentrations with small mean (median) biases of 0.05–0.08 (0.63–0.99)  $\mu\text{g}/\text{m}^3$  during different hours throughout the day.

*[Please insert Figure 8 here]*

255 We also compared Himawari-8-derived and ground-based PM<sub>2.5</sub> diurnal variations from all available monitoring stations in China and three typical urban clusters (Figure 9). Hourly PM<sub>2.5</sub> concentrations observed by satellite are highly consistent with ground-based measurements, with a small difference within  $\pm 0.10$ , 0.11, 0.13, and 0.11  $\mu\text{g}/\text{m}^3$  in China and in each region, respectively. Moreover, the same diurnal variations of PM<sub>2.5</sub> pollution are seen during the day, i.e., they reach their maximum values at 260 10:00 or 11:00 and are lower at sunrise and sunset. These results illustrate that the diurnal PM<sub>2.5</sub> variations derived from Himawari-8 are reasonable compared to ground-based measurements.

*[Please insert Figure 9 here]*

We investigated the time series of the daily performance of the STLG model in estimating hourly PM<sub>2.5</sub> concentrations in China. The number of data samples varies on a daily basis, with an average of 3975 265 per day and with more than 83% of all days having more than 2000 (Figure 10). The large gap in the number of data samples is mainly caused by different degrees of cloud contamination in the satellite

aerosol products for different days. The STLG model captures well the hourly PM<sub>2.5</sub> values on most days, with an average out-of-sample  $R^2$  of 0.73 and average RMSE and MAE values of 13.06  $\mu\text{g}/\text{m}^3$  and 8.53  $\mu\text{g}/\text{m}^3$ , respectively. In general, hourly PM<sub>2.5</sub> estimates are more reliable on approximately 79%  
270 (CV- $R^2 > 0.7$ ), 70% (RMSE < 15  $\mu\text{g}/\text{m}^3$ ), and 74% (MAE < 10  $\mu\text{g}/\text{m}^3$ ) of the days in the year. The model performance also varies greatly at the seasonal level, with average CV- $R^2$  values of 0.82, 0.71, 0.87, and 0.86, and average RMSE values of 14.55, 9.63, 11.83, and 17.57  $\mu\text{g}/\text{m}^3$  in spring, summer, autumn, and winter, respectively (Figure 11). In general, the overall uncertainty of PM<sub>2.5</sub> estimates increases at the beginning and at the end of the year, likely due to the harsher environmental conditions  
275 (e.g., low humidity and less precipitation) and more intense human activities (e.g., coal heating and straw burning) in winter and spring.

*[Please insert Figures 10 and 11 here]*

We have evaluated temporally synthesized PM<sub>2.5</sub> data from the hourly data samples at each monitoring station for the year 2018 (Figure 12). Daily mean PM<sub>2.5</sub> estimates are highly correlated to those  
280 calculated from surface observations ( $R^2 = 0.91$ ), and the average RMSE (MAE) value is 10.11 (6.39)  $\mu\text{g}/\text{m}^3$ . This suggests that the STLG model can capture daily PM<sub>2.5</sub> variations more accurately. Note that daily synthetic PM<sub>2.5</sub> data derived from geostationary satellites have a higher temporal frequency than data derived from sun-synchronous satellites. In general, PM<sub>2.5</sub> synthetic values also have high  
285 accuracies and low estimation uncertainties (e.g.,  $R^2 = 0.98$ , RMSE = 1.6–3.3  $\mu\text{g}/\text{m}^3$ , MAE = 1.1–2.3  $\mu\text{g}/\text{m}^3$ ) from monthly to annual scales, allowing for a better description of spatiotemporal distributions and variations of PM<sub>2.5</sub> pollution across China.

*[Please insert Figure 12 here]*

## 3.2 Spatiotemporal characteristics

### 3.2.1 Diurnal variations

290 Figure 13 shows Himawari-8-derived hourly mean near-surface PM<sub>2.5</sub> concentrations from 08:00 to 17:00 local time in 2018 across mainland China. They do not cover western Xinjiang and Tibet due to the limitation of satellite scanning. PM<sub>2.5</sub> pollution varies diurnally across China, being at an overall low

level at sunrise ( $\sim 29.94 \pm 10.91 \mu\text{g}/\text{m}^3$ ). With the increase in human activities, air pollution becomes more severe over time, reaching a peak at around 10:00–11:00 local time in China ( $\sim 36 \pm 13 \mu\text{g}/\text{m}^3$ ).

295 These high levels of pollution can last several hours. As the day progresses, human activities subside, and atmospheric fine particles settle on surfaces. PM<sub>2.5</sub> concentrations thus decrease towards sunset in most areas in China ( $\sim 23.21 \pm 9.73 \mu\text{g}/\text{m}^3$ ). In general, air pollution in the morning (i.e., 08:00–12:00) is much more severe than in the afternoon (i.e., 13:00–17:00) in China, with morning PM<sub>2.5</sub> concentrations about 1.3 times higher than afternoon levels. This is related to the influence of varying BLHs (Z. Li et  
300 al., 2017; Su et al., 2018).

*[Please insert Figure 13 here]*

Table 2 summarizes the diurnal PM<sub>2.5</sub> variations in eastern China and three typical urban agglomerations. PM<sub>2.5</sub> pollution levels in eastern China are generally higher than the national level at each hour of the day due to the dense human population and intensive human activities. In the BTH region, PM<sub>2.5</sub> pollution varies greatly, with hourly PM<sub>2.5</sub> concentrations ranging from  $28.88 \pm 10.16 \mu\text{g}/\text{m}^3$  (10:00) to  $49.31 \pm 15.03 \mu\text{g}/\text{m}^3$  (16:00) and with differences exceeding  $20 \mu\text{g}/\text{m}^3$ . PM<sub>2.5</sub> pollution remained at a high level ( $> 42 \mu\text{g}/\text{m}^3$ ) before 12:00 and dropped to a lower level ( $< 29 \mu\text{g}/\text{m}^3$ ) after 16:00. This is closely related to people's daily activities and the production and life cycle of PM<sub>2.5</sub> during the day, as well as the change of boundary mixing as a function of the day (Lennartson et al.,  
305 2018; Wang and Christopher, 2003). Similar patterns and PM<sub>2.5</sub> pollution levels are seen in the YRD region. In general, the PRD region is less polluted in the morning but more severely polluted in the afternoon than the BTH region. Compared with the BTH and PRD regions, PM<sub>2.5</sub> pollution in the PRD region is much lower and shows a smaller diurnal difference, with hourly PM<sub>2.5</sub> values ranging from  $29.49 \pm 5.97 \mu\text{g}/\text{m}^3$  (11:00) to  $36.36 \pm 5.76 \mu\text{g}/\text{m}^3$  (08:00). Better natural conditions and fewer pollutant  
310 emissions mainly explain this (Su et al., 2018).

In general, our satellite-derived diurnal variations of PM<sub>2.5</sub> pollution agree well with ground-based observations at both national and regional levels but with generally lower PM<sub>2.5</sub> concentrations (Figure 9). The reason is that the PM<sub>2.5</sub> monitoring stations are unevenly distributed and vary greatly in the number of stations at the regional scale. Also, most sites are distributed in urban areas, leading to

320 inevitable overestimations due to urban-rural differences. However, satellite remote sensing can cope with this deficiency by generating spatially continuous PM<sub>2.5</sub> maps, providing more accurate information about the distribution and variations of PM<sub>2.5</sub> pollution.

*[Please insert Table 2 here]*

### **3.2.2 Seasonal and annual variations**

325 Seasonal PM<sub>2.5</sub> maps are synthesized from daily PM<sub>2.5</sub> maps from 2018 across China according to our previous approach (Wei et al., 2019a). Our results illustrate that PM<sub>2.5</sub> pollution varies greatly on a seasonal scale (Figure 14). Pollution levels are generally low and show similar spatial patterns in summer ( $\sim 22.86 \pm 7.05 \mu\text{g}/\text{m}^3$ ) and autumn ( $\sim 23.76 \pm 10.97 \mu\text{g}/\text{m}^3$ ) across China (Table 3). By contrast, it is much more severe in spring ( $\sim 32.84 \pm 11.49 \mu\text{g}/\text{m}^3$ ) and winter ( $\sim 39.04 \pm 16.32 \mu\text{g}/\text{m}^3$ ) across China,  
330 especially in the BTH and YRD regions in winter. The main reasons are the frequent sandstorms and the long-distance transmission of sand and dust in spring, and the burning of coal and fossil fuels for heating in winter, leading to more pollutant emissions in northern China.

*[Please insert Figure 14 and Table 3 here]*

PM<sub>2.5</sub> pollution also shows significant spatial heterogeneities across China (Figure 15), with an annual  
335 mean PM<sub>2.5</sub> concentration of  $28.99 \pm 10.31 \mu\text{g}/\text{m}^3$  in 2018 (Table 3). High pollution levels are always observed in the Hebei, Shandong, Jiangsu, Anhui, Henan, Hubei, and Sichuan provinces. Interactions between intensive human activities, adverse stagnant weather (e.g., low BLHs and low winds), and special terrain (e.g., basin) can increase anthropogenic aerosols (Z. Chen et al., 2008; X. Wang et al., 2018). By contrast, PM<sub>2.5</sub> pollution is relatively light in the northeast (e.g., Heilongjiang and Jilin  
340 provinces), the southwest (e.g., Tibet and Yunnan provinces), and the eastern coastal areas of China (e.g., Zhejiang and Fujian provinces). These provinces are sparsely populated or experience meteorological conditions favorable for dispersing pollution (Su et al., 2018).

*[Please insert Figure 15 here]*

### **3.3 Discussion**

345 **3.3.1 Comparison with traditional models**

We first compared results from the STLG model with results from five widely used statistical regression models employed for estimating PM<sub>2.5</sub> in China using the same input dataset (Table 4). The multivariate linear regression (MLR) model performs the worst due to the complex nonlinear PM<sub>2.5</sub>-AOD relationship. The GWR model performs better because it takes into account the spatial characteristics of PM<sub>2.5</sub> pollution. The generalized additive model (GAM) and the LME model show overall improved performances, with decreasing estimation uncertainties because of their nonlinear characteristics and stronger data regression abilities. The two-stage model outperforms the GAM and MLE models, with higher CV-R<sup>2</sup> values and smaller estimation uncertainties, by combining the advantages of the GWR and LME models. Our model performs better than all of the traditional statistical regression models considered, mainly due to its stronger data-mining ability.

*[Please insert Table 4 here]*

The first six rows of Table 5 show the accuracies and efficiencies of six tree-based machine-learning models when estimating PM<sub>2.5</sub> in China using the same input dataset. The Decision Tree (DT; Quinlan, 1986) is a traditional, frequently used, supervised learning classification method. Although the training 360 speed is the fastest, and the memory consumption is the least, it has the worst performance because of the simple single classifier. The model performances of ensemble-learning approaches, i.e., GBDT (Friedman, 2001), RF (Breiman, 2001), extremely randomized trees (ERT; Geurts et al., 2006), and XGBoost (Chen & Guestrin, 2016), can be significantly improved by combining several weak classifiers into a strong classifier. Among them, the ERT model yields a higher estimation accuracy and 365 a stronger spatial prediction ability than other ensemble-learning models. The LightGBM model (Ke et al., 2017) performs the best, with the highest accuracy and smallest uncertainty among all tree-based machine-learning approaches considered.

*[Please insert Table 5 here]*

The model efficiency differs among these models due to the large differences in the algorithm design 370 frameworks. These tree-based, machine-learning models can be divided into two categories. The DT,

RF, and ERT models fall into the "bagging" category, which synthesizes multiple independent and unrelated weak classifiers into a strong classifier. It allows for work in parallel, which can save much time but may need more computer memory. The GBDT, XGBoost, and LightGBM models fall into the "boosting" category, which synthesizes multiple interdependent and related weak classifiers into a strong classifier. They can only work in serial, which may take much time but not too much memory. In general, the STGB model is the most time-consuming, while the STET model is the most memory-consuming. By contrast, the LightGBM model runs very fast and consumes very little computer memory, benefiting from a series of algorithm optimizations (Ke et al., 2017).

After considering spatiotemporal variations, all the newly defined space-time tree-based machine-learning approaches (i.e., STDT, STGB, STXB, STRF, STET, and STLG) show significant improvements in both overall estimation accuracy and spatial prediction ability in estimating hourly PM<sub>2.5</sub> concentrations with reference to their original models. This further illustrates the importance of including spatiotemporal information when constructing PM<sub>2.5</sub>–AOD relationships. More importantly, the training speed of these models did not decrease much, and the memory consumption did not increase much either. In general, the STLG model shows the best performance with a high efficiency (i.e., training speed = 46 s, memory usage = 0.60 GB) among all the space-time, tree-based machine-learning models. Therefore, our new STLG model is highly valuable for accurate and fast air pollution monitoring, in particular for our future study extended to the global scale.

### 390 3.3.2 Comparison with related studies

We compared Himawari-8-based hourly PM<sub>2.5</sub> estimates at regional and national scales in China with previous related studies (Table 6). Local hourly PM<sub>2.5</sub> concentrations retrieved from our national-scale model are more accurate than those derived from the models developed separately in local areas, e.g., the LME model (W. Wang et al., 2017), the GWR, SVR, RF, and DNN models in the BTH region (Sun et al., 2019), and the two-stage RF and DNN models in the YRD region (Fan et al., 2020; Tang et al., 2019). Our model also outperforms most of the statistical regression models and machine-learning models focused on the entirety of China, e.g., the I-LME, IGTWR, RF, Adaboost, XGBoost, and their stacked models in China (J. Chen et al., 2019; Liu et al., 2019; Xue et al., 2020; T. Zhang et al., 2019).

This is due to the stronger data-mining ability, considering key spatial and temporal information about  
400 air pollution (ignored in previous studies), and introduces more comprehensive factors that affect PM<sub>2.5</sub> pollution (e.g., emission inventories).

*[Please insert Table 6 here]*

#### 4. Summary and conclusion

PM<sub>2.5</sub> has a great impact on the atmospheric environment and is also used as a key indicator in  
405 environmental health studies. It varies diurnally, affected by both natural and human factors. Previous studies have been based on data from sun-synchronous satellites, which can monitor air pollution at coarse temporal scales (i.e., daily) while high-temporal-resolution and accurate information on PM<sub>2.5</sub> are needed. In this study, the Himawari-8/AHI hourly AOD product is employed to address this issue. Moreover, considering the large volume of input data and the large errors in PM<sub>2.5</sub> estimation using  
410 traditional methods, an efficient and accurate space-time Light Gradient Boosting Machine (i.e., STLG) model has been developed. It utilizes meteorological, human, land use, and topographical parameters and is implemented at 5-km resolution and hourly time scale to generate PM<sub>2.5</sub> information over China. The hourly PM<sub>2.5</sub> estimates are evaluated against surface observations, and PM<sub>2.5</sub> spatiotemporal variations are also investigated.

415 The STLG model predicts hourly PM<sub>2.5</sub> values accurately, with high out-of-sample (out-of-station) CV- $R^2$  values of ~0.81–0.85 (~0.76–0.81) and low RMSE values of ~11.24–15.56 (~12.49–17.61)  $\mu\text{g}/\text{m}^3$  throughout the day. The model can also produce daily (e.g.,  $R^2 = 0.91$ , RMSE = 10.11  $\mu\text{g}/\text{m}^3$ ), monthly, seasonal, and annual mean PM<sub>2.5</sub> values (e.g.,  $R^2 = 0.98$ , RMSE = 1.6–3.3  $\mu\text{g}/\text{m}^3$ ). PM<sub>2.5</sub> varies diurnally in most areas of mainland China, where PM<sub>2.5</sub> concentrations reach a maximum at 10 a.m. and  
420 are generally low at sunrise and sunset on a given day. PM<sub>2.5</sub> also varies greatly on a seasonal basis, where winter and summer experience the highest and lowest air pollution levels, respectively. Comparison results suggest that the proposed model is more accurate than traditional statistical regression models, other tree-based machine learning models, and various models developed in previous studies. Overall, the STLG model is more efficient, with faster training speed and less memory

425 consumption. These results illustrate that this algorithm can be useful for real-time monitoring of PM<sub>2.5</sub>  
pollution in China.

## **Data availability**

PM<sub>2.5</sub> measurements are available at <http://www.cnemc.cn>, the Himawari-8 AOD product is available at  
430 <ftp://ptree.jaxa.jp>, ERA5 reanalysis products are available at <https://cds.climate.copernicus.eu/>, the  
MODIS product is available at <https://search.earthdata.nasa.gov/>, and the LandScan<sup>TM</sup> product is  
available at <https://landscan.ornl.gov/>.

## **Author contribution**

435 JW designed the research and wrote the initial draft of this manuscript. ZL, RP, JW, and LS reviewed  
and edited the paper. RL and WX helped to process the data. MC copyedited the article. All authors  
made substantial contributions to this work.

## **Competing interests**

440 The authors declare that they have no conflict of interest.

## **Acknowledgements**

We would like to thank Dr. Qiang Zhang at Tsinghua University for providing MEIC pollution  
emission data for China.

445

## **Financial support**

This research has been supported by the National Key R&D Program of China (2017YFC1501702) and  
the National Natural Science Foundation of China (42030606).

450 **References**

An, Z., and Coauthors. Severe haze in northern China: a synergy of anthropogenic emissions and atmospheric processes. *Proceedings of the National Academy of Sciences*, 116(18), 8657–8666, 2019.

455 Baez-Villanueva, O., and Coauthors. RF-MEP: a novel random forest method for merging gridded precipitation products and ground-based measurements. *Remote Sensing of Environment*, 239(111606), 2020.

Behrens, T., Schmidt, K., Viscarra, R., Gries, P., Scholten, T., & Macmillan, R. Spatial modelling with Euclidean distance fields and machine learning. *European Journal of Soil Science*, 69, 757–770, 2018.

460 Bessho, K., Date, K., Hayashi, M., Ikeda, A., & Yoshida, R. An introduction to Himawari-8/9—Japan's new-generation geostationary meteorological satellites. *Journal of the Meteorological Society of Japan*, 2016, 94(2), 151–183, 2016.

Breiman, L. Random forests. *Machine Learning*, 45, 5–32, 2001.

465 Chan, C., & Yao, X. Air pollution in megacities in China. *Atmospheric Environment*, 42(1), 1–42, 2008.

Chen, T., & Guestrin, C. XGBoost: a scalable tree boosting system. *Proceedings of the 22nd ACM SIGKDD International Conference on Knowledge Discovery and Data Mining*, 785–794, 2016.

470 Chen, J., Yin, J., Zang, L., Zhang, T., & Zhao, M. Stacking machine learning model for estimating hourly PM<sub>2.5</sub> in China based on Himawari-8 aerosol optical depth data. *Science of the Total Environment*, 697, 134021, 2019.

Chen, Z., Cheng, S., Li, J., Guo, X., Wang, W., & Chen, D. Relationship between atmospheric pollution processes and synoptic pressure patterns in northern China. *Atmospheric Environment*, 42(24), 6078–6087, 2008.

475 Delfino, R.J., Sioutas, C., & Malik, S. Potential role of ultrafine particles in associations between airborne particle mass and cardiovascular health. *Environmental Health Perspectives*, 113(8), 934–946, 2005.

Dobson, J., Bright, E., Coleman, P., Durfee, R., & Worley, B. A global population database for estimating populations at risk. *Photogrammetric Engineering & Remote Sensing*, 66(7), 2000.

Fan, W., Qin, K., Cui, Y., Li, D., & Bilal, M. Estimation of hourly ground-level PM<sub>2.5</sub> concentration based on Himawari-8 apparent reflectance. *IEEE Transactions on Geoscience and Remote Sensing*, 59(1), 76–85, 2020. <https://doi.org/10.1109/TGRS.2020.2990791>

480 Friedman, J. Greedy function approximation: a gradient boosting machine. *Annals of Statistics*, 29(5), 1189–1232, 2001.

Geurts, P., Ernst, D., & Wehenkel, L. Extremely randomized trees. *Machine Learning*, 63, 3–42, 2006.

485 Giles, D., Sinyuk, A., Sorokin, M., Schafer, J., Smirnov, A., Slutsker, I., Eck, T., Holben, B., Lewis, J., Campbell, J., Welton, E., Korkin, S., & Lyapustin, A. Advancements in the Aerosol Robotic Network (AERONET) Version 3 database – automated near-real-time quality control algorithm with improved cloud screening for Sun photometer aerosol optical depth (AOD) measurements. *Atmospheric Measurement Techniques*, 12, 169–209, 2019.

490 Gui, K., and Co-authors. Construction of a virtual PM<sub>2.5</sub> observation network in China based on high-density surface meteorological observations using the Extreme Gradient Boosting model. *Environment International*, 141, 105801, 2020.

Huang, R., and Co-authors. High secondary aerosol contribution to particulate pollution during haze events in China. *Nature*, 514, 218–222, 2014.

495 Jacob, D., & Winner, D. Effect of climate change on air quality. *Atmospheric Environment*, 43(1), 51–63, 2009.

Kampa, M., & Castanas, E. Human health effects of air pollution. *Environmental Pollution*, 151(2), 362–367, 2008.

500 Ke, G., Meng, Q., Finley, T., Wang, T., Chen, W., Ma, W., Ye, Q., & Liu, T. LightGBM: a highly efficient gradient boosting decision tree. In *Advances in Neural Information Processing Systems*, 3149–3157, 2017.

Kim, K., Kabir, E., & Kabir, S. A review on the human health impact of airborne particulate matter. *Environment International*, 74, 136–143, 2015.

505 Lelieveld, J., Evans, J., Fnais, M., Giannadaki, D., & Pozzer, A. The contribution of outdoor air pollution sources to premature mortality on a global scale. *Nature*, 525, 367–371, 2015.

Lennartson, E., Wang, J., Gu, J., Castro Garcia., L., Ge, C., Gao, M., Choi, M., Saide, P., Carmichael, G., Kim, J., & Janz, S. Diurnal variation of aerosol optical depth and PM<sub>2.5</sub> in south Korea: a synthesis from AERONET, satellite (GOCI), KORUS-AQ observation, and WRF-Chem model, *Atmospheric Chemistry and Physics*, 18, 15125–15144, 2018.

510 Letu, H., and Coauthors. High-resolution retrieval of cloud microphysical properties and surface solar radiation using Himawari-8/AHI next-generation geostationary satellite. *Remote Sensing of Environment*, 239, 111583, 2020.

Li, M., Liu, H., Geng, G., Hong, C., Liu, F., Song, Y., Tong, D., Zheng, B., Cui, H., Man, H., Zhang, Q., & He, K. Anthropogenic emission inventories in China: a review, *National Science Review*, 4, 515 834-866, doi: 10.1093/nsr/nwx150, 2017.

Li, Z., Guo, J., Ding, A., Liao, H., Liu, J., Sun, Y., Wang, T., Xue, H., Zhang, H., & Zhu, B. Aerosols and boundary-layer interactions and impact on air quality. *National Science Review*, 4, 810–833, 2017.

520 Li, Z., Xu, H., Li, K., Li, D., Xie, Y., Li, L., Zhang, Y., Gu, X., Zhao, W., Tian, Q., Deng, R., Su, X., Huang, B., Qiao, Y., Cui, W., Hu, Y., Gong, C., Wang, Y., Wang, X., Wang, J., Du, W., Pan, Z., Li, Z., & Bu, D. Comprehensive study of optical, physical, chemical, and radiative properties of total columnar atmospheric aerosols over China: an overview of Sun–Sky Radiometer Observation Network (SONET) measurements. *Bulletin of the American Meteorological Society*, 99, 739–755, 2018.

525 Li, Z., and Coauthors. East Asian Study of Tropospheric Aerosols and their Impact on Regional Clouds, Precipitation, and Climate (EAST-AIRCPC). *Journal of Geophysical Research: Atmospheres*, 124, 13,026–13,054, 2019.

Liu, J., Weng, F., Li, Z., & Cribb, M. Hourly PM<sub>2.5</sub> estimates from a geostationary satellite based on an ensemble learning algorithm and their spatiotemporal patterns over central East China. *Remote Sensing*, 11(18), 2120, 2019.

Liu, Y., Sarnat, J., Kilaru, V., Jacob, D., & Koutrakis, P. Estimating ground-level PM<sub>2.5</sub> in the eastern United States using satellite remote sensing. *Environmental Science & Technology*, 39(9), 3269–78, 2005.

Liu, Y., Franklin, M., Kahn, R., & Koutrakis, P. Using aerosol optical thickness to predict ground-level PM<sub>2.5</sub> concentrations in the St. Louis area: a comparison between MISR and MODIS. *Remote Sensing of Environment*, 107(1–2), 33–44, 2007.

Ma, Z., Hu, X., Huang, L., Bi, J., & Liu, Y. Estimating ground-level PM<sub>2.5</sub> in China using satellite remote sensing. *Environmental Science and Technology*, 48(13), 7436–7444, 2014.

Quinlan, J. Induction on decision tree. *Machine Learning*, 1, 81–106, 1986.

Ramanathan, V., & Feng, Y. Air pollution, greenhouse gases and climate change: global and regional perspectives. *Atmospheric Environment*, 43(1), 37–50, 2009.

Rodriguez, J. D., Perez, A., & Lozano, J. A. Sensitivity analysis of k-fold cross-validation in prediction error estimation. *IEEE Transactions on Pattern Analysis and Machine Intelligence*, 32, 569–575, 2010.

Shi, H. Best-first decision tree learning. PhD thesis, The University of Waikato, 2007.

Su, T., Li, Z., & Kahn, R. Relationships between the planetary boundary layer height and surface pollutants derived from lidar observations over China: regional pattern and influencing factors. *Atmospheric Chemistry and Physics*, 18, 15,921–15,935, 2018.

Sun, Y., and Coauthors. The air-borne particulate pollution in Beijing—concentration, composition, distribution and sources. *Atmospheric Environment*, 38(35), 5991–6004, 2004.

Sun, Y., Zeng, Q., Geng, B., Lin, X., Sude, B., & Chen, L. Deep learning architecture for estimating hourly ground-level PM<sub>2.5</sub> using satellite remote sensing. *IEEE Geoscience and Remote Sensing Letters*, 16(9), 1343–1347, 2019.

Tang, D., Liu, D., Tang, Y., Seyler, B., Deng, X., & Zhan, Y. Comparison of GOCI and Himawari-8 aerosol optical depth for deriving full coverage hourly PM<sub>2.5</sub> across the Yangtze River Delta. *Atmospheric Environment*, 217, 116973, 2019.

van Donkelaar, A., Martin, R., & Park, R. Estimating ground-level PM<sub>2.5</sub> using aerosol optical depth determined from satellite remote sensing. *Journal of Geophysical Research: Atmospheres*, 111(D21), 2006.

560 Wang, J., & Christopher, S. Intercomparison between satellite-derived aerosol optical thickness and PM<sub>2.5</sub> mass: Implication for air quality studies, *Geophysical Research Letters*, 30, 2095, doi:10.1029/2003GL018174, 2003.

Wang, W., Mao, F., Du, L., Pan, Z., Gong, W., & Fang, S. Deriving hourly PM<sub>2.5</sub> concentrations from Himawari-8 AODs over Beijing-Tianjin-Hebei in China. *Remote Sensing*, 9(8), 858, 2017.

565 Wang, X., Dickinson, R., Su, L., Zhou, C., & Wang, K. PM<sub>2.5</sub> pollution in China and how it has been exacerbated by terrain and meteorological conditions. *Bulletin of the American Meteorological Society*, 99 (1), 105–119, 2018.

Wei, J., Huang, W., Li, Z., Xue, W., Peng, Y., Sun, L., & Cribb, M. Estimating 1-km-resolution PM<sub>2.5</sub> concentrations across China using the space-time random forest approach. *Remote Sensing of Environment*, 231, 111221, 2019a.

570 Wei, J., Li, Z., Sun, L., Peng, Y., Zhang, Z., Li, Z., Su, T., Feng, L., Cai, Z., & Wu, H. Evaluation and uncertainty estimate of the next-generation geostationary meteorological Himawari-8/AHI aerosol products. *Science of the Total Environment*, 692, 879–891, 2019b.

Wei, J., Li, Z., Peng, Y., & Sun, L. MODIS Collection 6.1 aerosol optical depth products over land and 575 ocean: validation and comparison. *Atmospheric Environment*, 201, 428–440, 2019c.

Wei, J., Li, Z., Cribb, M., Huang, W., Xue, W., Sun, L., Guo, J., Peng, Y., Li, J., Lyapustin, A., Liu, L., Wu, H., & Song, Y. Improved 1-km resolution PM<sub>2.5</sub> estimates across China using enhanced space-time extremely randomized trees. *Atmospheric Chemistry and Physics*, 20(6), 3273–3289, 2020.

580 Wei, J., Li, Z., Lyapustin, A., Sun, L., Peng, Y., Xue, W., Su, T., & Cribb, M. Reconstructing 1-km-resolution high-quality PM<sub>2.5</sub> data records from 2000 to 2018 in China: spatiotemporal variations and policy implications. *Remote Sensing of Environment*, 252, 112136, 2021a.

Wei, J., Li, Z., Sun, L., Xue, X., Ma, Z., Liu, L., Fan, T., & Cribb, M. Extending the EOS long-term PM<sub>2.5</sub> data records since 2013 in China: application to the VIIRS Deep Blue aerosol

products. *IEEE Transactions on Geoscience and Remote Sensing*, 2021b.

<https://doi.org/10.1109/TGRS.2021.3050999>

Wu, J., Yao, F., Si, M., & Li, W. VIIRS-based remote sensing estimation of ground-level PM<sub>2.5</sub> concentrations in Beijing–Tianjin–Hebei: a spatiotemporal statistical model. *Remote Sensing of Environment*, 184, 316–328, 2016.

590 Xue, Y., and Co-authors. Hourly PM<sub>2.5</sub> estimation over central and eastern China based on Himawari-8 data. *Remote Sensing*, 12(5), 855, 2020.

Yao, F., Wu, J., Li, W., & Peng, J. A spatially structured adaptive two-stage model for retrieving ground-level PM<sub>2.5</sub> concentrations from VIIRS AOD in China. *ISPRS Journal of Photogrammetry and Remote Sensing*, 151, 263–276, 2019.

595 Yoshida, M., Kikuchi, M., Nagao, T., Murakami, H., Nomaki, T., & Higurashi, A. Common retrieval of aerosol properties for imaging satellite sensors. *Journal of the Physical Society of Japan*, 96b, 193–209, 2018.

Zhang, Q., Streets, D., He, K., & Klimont, Z. Major components of China's anthropogenic primary particulate emissions. *Environmental Research Letters*, 2, No. 045027, 2007.

600 Zhang, Q., Zheng, Y., Tong, D., Shao, M., & Hao, J. Drivers of improved PM<sub>2.5</sub> air quality in china from 2013 to 2017. *Proceedings of the National Academy of Sciences*, 201907956, 2019.

Zhang, T., Zang, L., Wan, Y., Wang, W., & Zhang, Y. Ground-level PM<sub>2.5</sub> estimation over urban agglomerations in China with high spatiotemporal resolution based on Himawari-8. *Science of the Total Environment*, 676, 535–544, 2019.

605 Zhang, T., He, W., Zheng, H., Cui, Y., Song, H., & Fu, S. Satellite-based ground PM<sub>2.5</sub> estimation using a gradient boosting decision tree. *Chemosphere*, 128801, 2020.

Zheng, B., Tong, D., Li, M., Liu, F., Hong, C., Geng, G., Li, H., Li, X., Peng, L., Qi, J., Yan, L., Zhang, Y., Zhao, H., Zheng, Y., He, K., & Zhang, Q. Trends in China's anthropogenic emissions since 2010 as the consequence of clean air actions, *Atmospheric Chemistry and Physics*, 18, 14095–14111, doi: 10.5194/acp-18-14095-2018, 2018.

## Tables

**Table 1.** Summary of datasets and sources used in this study.

Dataset	Variable	Content	Unit	Spatial Resolution	Temporal Resolution	Data Source
PM <sub>2.5</sub>	PM <sub>2.5</sub>	PM <sub>2.5</sub>	µg/m <sup>3</sup>	in situ	Hourly	CNEMC
AOD	AOD	Himawari-8 AOD	-	5 km × 5 km	Hourly	Himawari-8
Meteorology	ET	Total evaporation	mm	0.1°×0.1°		
	SP	Surface pressure	hPa	0.1°×0.1°		
	TEM	2-m temperature	K	0.1°×0.1°		
	WU	10-m u-component of wind	m/s	0.1°×0.1°	Hourly	ERA5
	WV	10-m v-component of wind	m/s	0.1°×0.1°		
	BLH	Boundary-layer height	m	0.25°×0.25°		
	RH	Relative humidity	%	0.25°×0.25°		
Emissions	NH <sub>3</sub>	Ammonia	Mg/grid			
	NO <sub>x</sub>	Nitrogen oxides	Mg/grid			
	SO <sub>2</sub>	Sulfur dioxide	Mg/grid	0.25°×0.25°	Monthly	MEIC
	VOC	Volatile organic compounds	Mg/grid			
	PM	PM, coarse	Mg/grid			
Land cover	NDVI	NDVI	-	0.05°×0.05°	Monthly	MOD13C2
Topography	DEM	Surface elevation	m	90 m × 90 m	-	SRTM
Population	POP	Ambient population	-	1 km × 1 km	Yearly	LandScan <sup>TM</sup>

**Table 2.** Hourly mean PM<sub>2.5</sub> concentrations ( $\mu\text{g}/\text{m}^3$ ) in 2018 in China, eastern China (ECHN), the Beijing-Tianjin-Hebei (BTH) region, the Yangtze River Delta (YRD), and the Pearl River Delta (PRD).

Time	China	ECHN	BTH	YRD	PRD
08:00	29.94 $\pm$ 10.91	31.97 $\pm$ 11.55	42.46 $\pm$ 12.97	38.60 $\pm$ 10.57	29.34 $\pm$ 5.01
09:00	33.37 $\pm$ 12.59	36.29 $\pm$ 13.52	47.32 $\pm$ 15.04	43.55 $\pm$ 11.27	34.81 $\pm$ 5.46
10:00	35.67 $\pm$ 13.53	38.56 $\pm$ 14.05	49.31 $\pm$ 15.03	44.72 $\pm$ 11.17	35.48 $\pm$ 5.47
11:00	35.63 $\pm$ 13.05	38.72 $\pm$ 13.53	49.10 $\pm$ 13.77	44.27 $\pm$ 10.55	36.36 $\pm$ 5.76
12:00	31.23 $\pm$ 11.74	35.10 $\pm$ 12.47	42.38 $\pm$ 12.86	41.37 $\pm$ 9.77	34.56 $\pm$ 5.72
13:00	28.45 $\pm$ 11.40	32.23 $\pm$ 11.73	37.70 $\pm$ 11.55	39.36 $\pm$ 9.22	33.33 $\pm$ 5.48
14:00	26.36 $\pm$ 11.18	30.14 $\pm$ 11.09	34.32 $\pm$ 11.81	37.31 $\pm$ 8.59	32.05 $\pm$ 5.50
15:00	24.25 $\pm$ 10.06	28.67 $\pm$ 10.21	31.95 $\pm$ 11.26	36.77 $\pm$ 8.13	30.34 $\pm$ 5.43
16:00	23.63 $\pm$ 9.26	27.38 $\pm$ 9.15	29.82 $\pm$ 10.13	32.84 $\pm$ 6.30	29.49 $\pm$ 5.97
17:00	23.21 $\pm$ 9.73	26.63 $\pm$ 8.93	28.88 $\pm$ 10.16	27.59 $\pm$ 4.39	31.56 $\pm$ 6.17
Morning	33.29 $\pm$ 11.59	36.15 $\pm$ 12.41	46.12 $\pm$ 13.29	42.50 $\pm$ 10.22	34.52 $\pm$ 4.63
Afternoon	25.11 $\pm$ 9.78	29.01 $\pm$ 9.70	32.53 $\pm$ 10.53	34.76 $\pm$ 6.66	31.42 $\pm$ 4.85

620 **Table 3.** Annual and seasonal mean PM<sub>2.5</sub> concentrations ( $\mu\text{g}/\text{m}^3$ ) in 2018 in China, eastern China  
 (ECHN), the Beijing-Tianjin-Hebei (BTH) region, the Yangtze River Delta (YRD), and the Pearl River  
 Delta (PRD).

Time	China	ECHN	BTH	YRD	PRD
Spring	32.84 $\pm$ 11.49	34.93 $\pm$ 10.95	45.75 $\pm$ 12.96	40.35 $\pm$ 9.55	33.97 $\pm$ 4.50
Summer	22.86 $\pm$ 7.05	24.16 $\pm$ 6.29	29.99 $\pm$ 7.46	26.16 $\pm$ 4.58	23.56 $\pm$ 3.18
Autumn	23.76 $\pm$ 10.97	28.64 $\pm$ 11.60	35.98 $\pm$ 11.20	35.97 $\pm$ 7.80	29.54 $\pm$ 4.43
Winter	39.04 $\pm$ 16.32	48.34 $\pm$ 17.47	48.36 $\pm$ 18.92	57.41 $\pm$ 16.88	43.92 $\pm$ 8.56
Annual	28.99 $\pm$ 10.31	32.56 $\pm$ 10.78	39.32 $\pm$ 11.74	38.64 $\pm$ 8.27	32.98 $\pm$ 4.53

**Table 4.** Comparison of the model performances of widely used models and the STLG model in estimating PM<sub>2.5</sub> from Himawari-8 data at 14:00 local time in 2018 in China (N = 162,840).

Model	Out-of-sample validation			Out-of-station validation		
	CV-R <sup>2</sup>	RMSE	MAE	CV-R <sup>2</sup>	RMSE	MAE
MLR	0.19	24.17	22.89	0.19	24.19	22.91
GWR	0.39	21.96	20.74	0.37	22.42	21.02
GAM	0.39	19.09	18.64	0.36	19.77	18.89
LME	0.50	18.91	17.34	0.48	19.06	17.95
Two-stage	0.58	17.60	15.71	0.54	17.99	16.01
STLG	0.85	13.09	8.11	0.81	14.63	9.29

**Table 5.** Comparison of the model performances of different tree-based machine-learning models and the STLG model using the same input data. Data are from 14:00 local time in 2018 in China (N = 162,840).

Model	Sample-based validation			Station-based validation			Speed (s)	Memory (GB)
	R <sup>2</sup>	RMSE	MAE	R <sup>2</sup>	RMSE	MAE		
DT	0.52	25.53	14.80	0.48	27.03	15.57	6	0.58
GBDT	0.65	20.03	13.17	0.61	21.20	14.10	94	0.59
XGBoost	0.73	17.94	10.78	0.68	19.59	11.93	456	0.69
RF	0.72	17.86	11.33	0.69	18.80	11.95	165	2.59
ERT	0.74	17.12	10.87	0.72	18.01	11.49	54	3.69
LightGBM	0.78	15.79	9.84	0.73	17.59	11.21	34	0.60
STDT	0.65	21.09	12.33	0.63	22.00	12.85	8	0.60
STGB	0.75	16.82	10.93	0.73	17.61	11.54	503	0.61
STXB	0.82	14.73	8.76	0.78	15.92	9.62	456	0.68
STRF	0.81	14.62	9.17	0.79	15.44	9.69	219	2.75
STET	0.82	14.42	8.95	0.80	15.30	9.55	77	4.25
STLG	0.85	13.09	8.11	0.81	14.63	9.29	46	0.60

**Table 6.** Comparison of model performances from previous studies in estimating hourly PM<sub>2.5</sub> concentrations in China.

Model	Model validation			Region	Reference
	R <sup>2</sup>	RMSE	MAE		
LME	0.86	24.5	14.2	BTH	W. Wang et al. (2017)
LME	0.63	29.0	18.1	BTH	Sun et al. (2019)
GWR	0.76	23.3	16.7		Sun et al. (2019)
SVR	0.77	21.5	12.3		Sun et al. (2019)
RF	0.82	20.3	12.1		Sun et al. (2019)
DNN	0.84	19.9	11.9		Sun et al. (2019)
two-stage RF	0.86	12.4	-	YRD	Tang et al. (2019)
DNN	0.86	14.3	-	YRD	Fan et al. (2020)
RF	0.82	19.6	12.2	China	J. Chen et al. (2019)
Adaboost	0.84	18.3	10.7		J. Chen et al. (2019)
XGBoost	0.84	18.1	11.4		J. Chen et al. (2019)
Stacked model	0.85	17.3	10.5		J. Chen et al. (2019)
RF	0.86	17.3	10.3	China	Liu et al. (2019)
I-LME	0.84	-	-	BTH	T. Zhang et al. (2019)
	0.80	-	-	YRD	
	0.74	-	-	PRD	
	0.82	-	-	China	
IGTWR	0.78	21.1	-	China	Xue et al. (2020)

## Figures

635

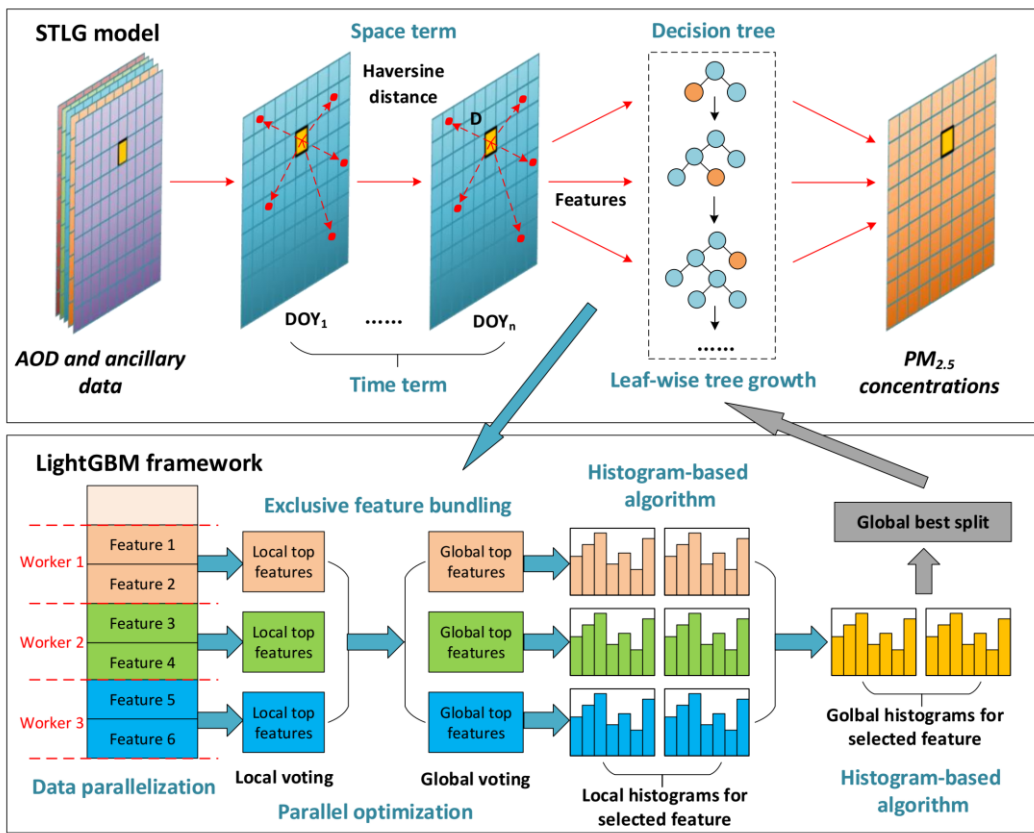
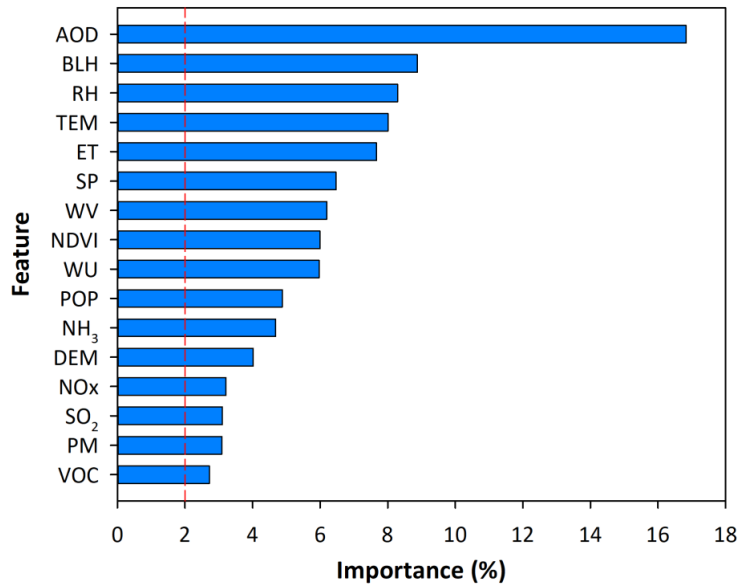
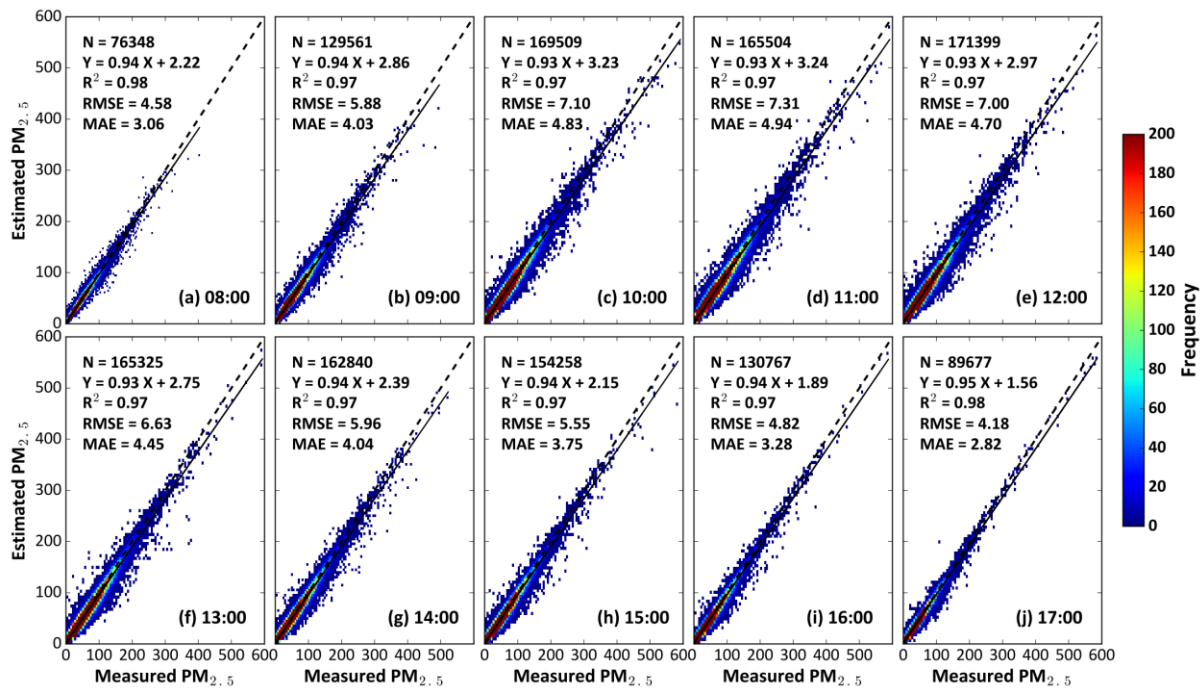


**Figure 1.** Schematics of the space-time LightGBM (STLG) model developed in this study (upper panel) and the framework of the original LightGBM model (bottom panel).

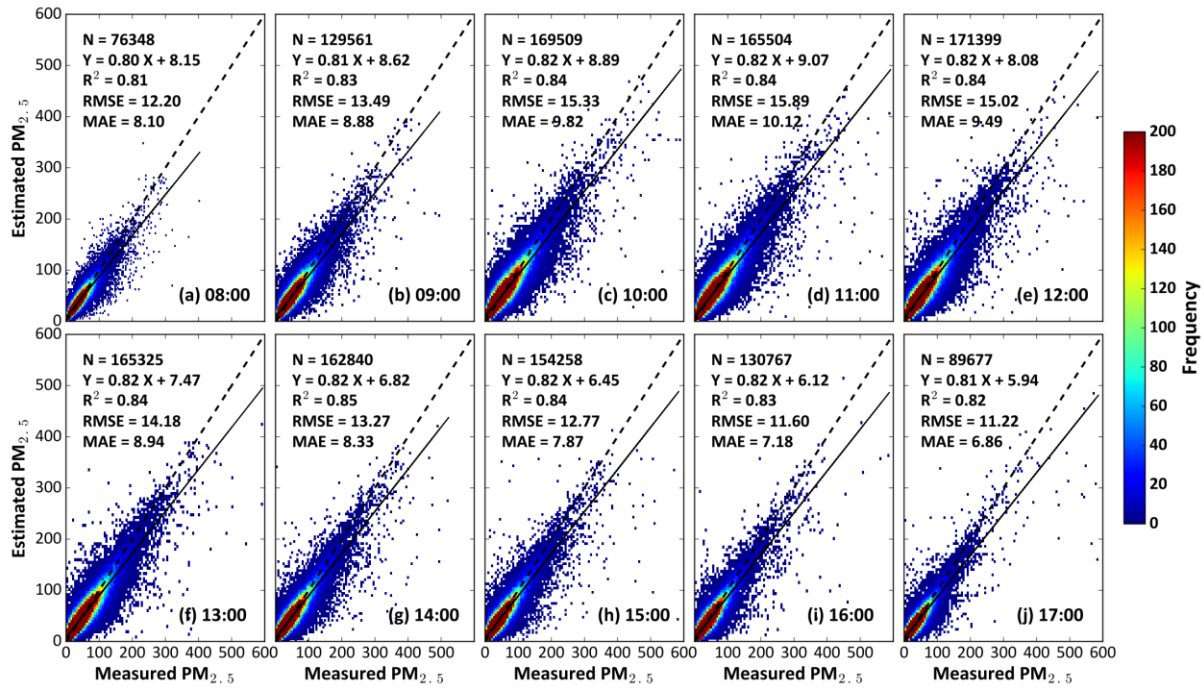


640

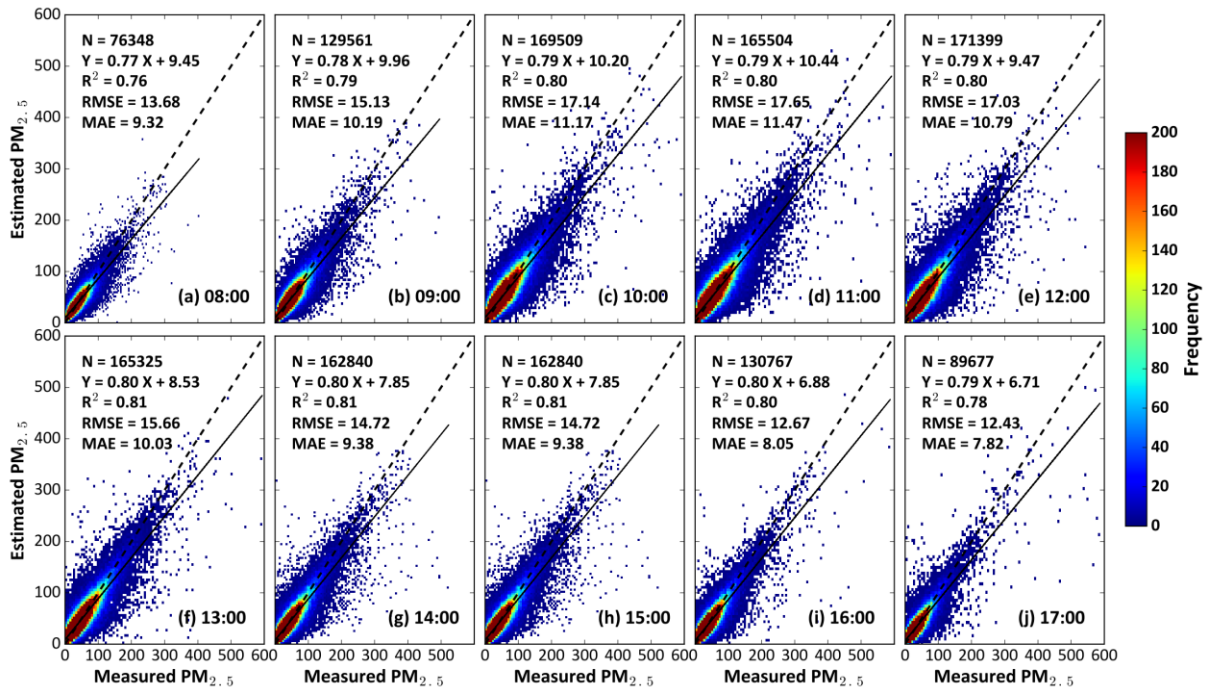
**Figure 2.** Sorted normalized importance (%) of each feature in the PM<sub>2.5</sub> estimation during the model construction.



645 **Figure 3.** Density scatterplots of model-fitted PM<sub>2.5</sub> estimates ( $\mu\text{g}/\text{m}^3$ ) at (a) 08:00, (b) 09:00, (c) 10:00, (d) 11:00, (e) 12:00, (f) 13:00, (g) 14:00, (h) 15:00, (i) 16:00, and (j) 17:00 local time in 2018 in China. Dashed lines denote 1:1 lines, and solid lines denote best-fit lines from linear regression.



650 **Figure 4.** Density scatterplots of out-of-sample cross-validation results of PM<sub>2.5</sub> estimates ( $\mu\text{g}/\text{m}^3$ ) at (a) 08:00, (b) 09:00, (c) 10:00, (d) 11:00, (e) 12:00, (f) 13:00, (g) 14:00, (h) 15:00, (i) 16:00, and (j) 17:00 local time in 2018 in China. Dashed lines denote 1:1 lines, and solid lines denote best-fit lines from linear regression.



655

**Figure 5.** Density scatterplots of out-of-station cross-validation results of PM<sub>2.5</sub> estimates ( $\mu\text{g}/\text{m}^3$ ) at (a) 08:00, (b) 09:00, (c) 10:00, (d) 11:00, (e) 12:00, (f) 13:00, (g) 14:00, (h) 15:00, (i) 16:00, and (j) 17:00 local time in 2018 in China. Dashed and solid lines denote 1:1 and best-fit lines from linear regression, respectively.

660

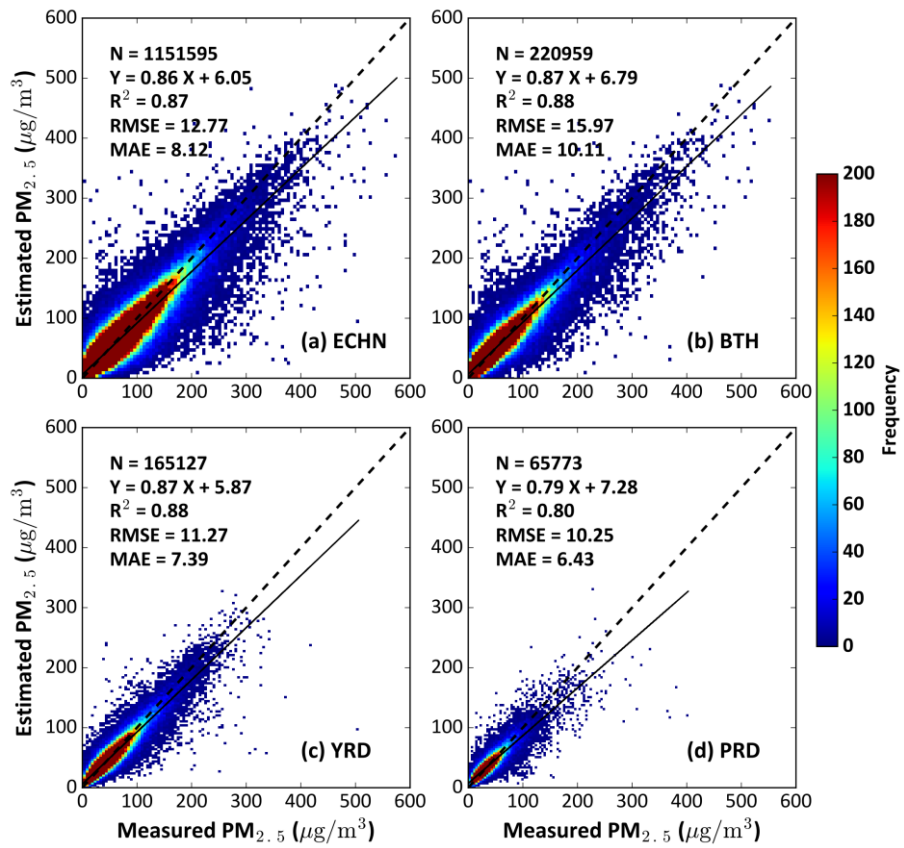
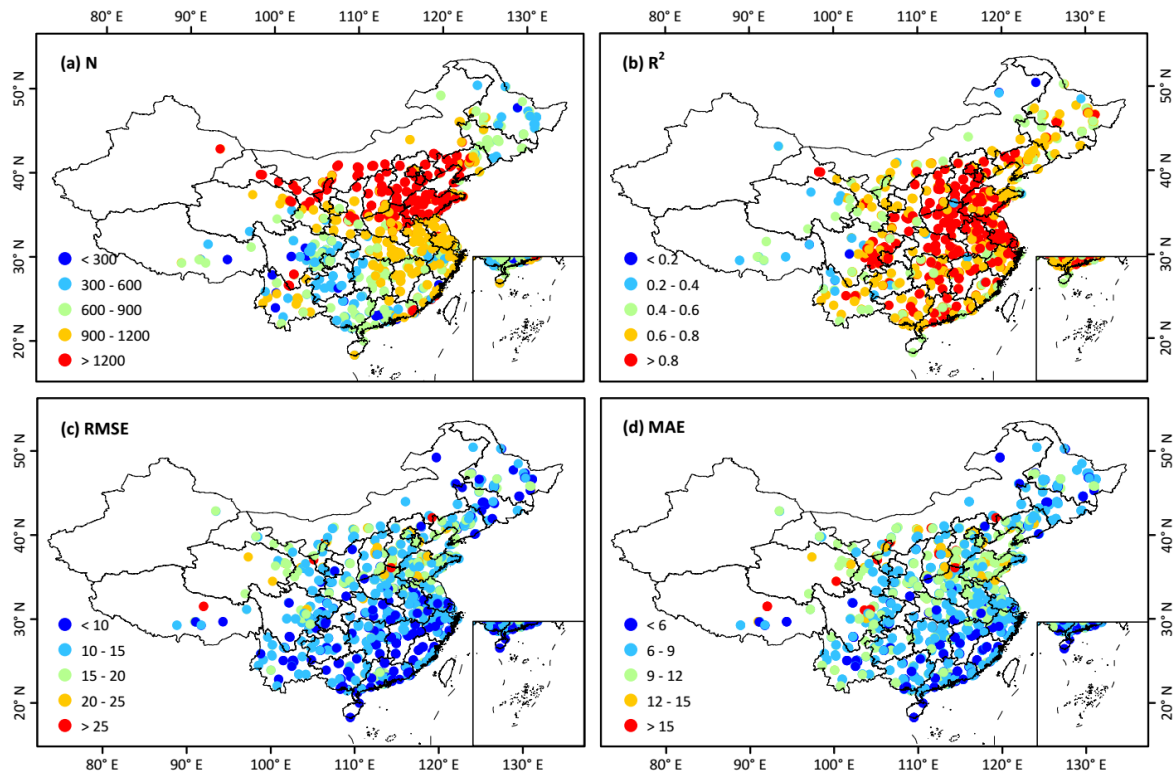
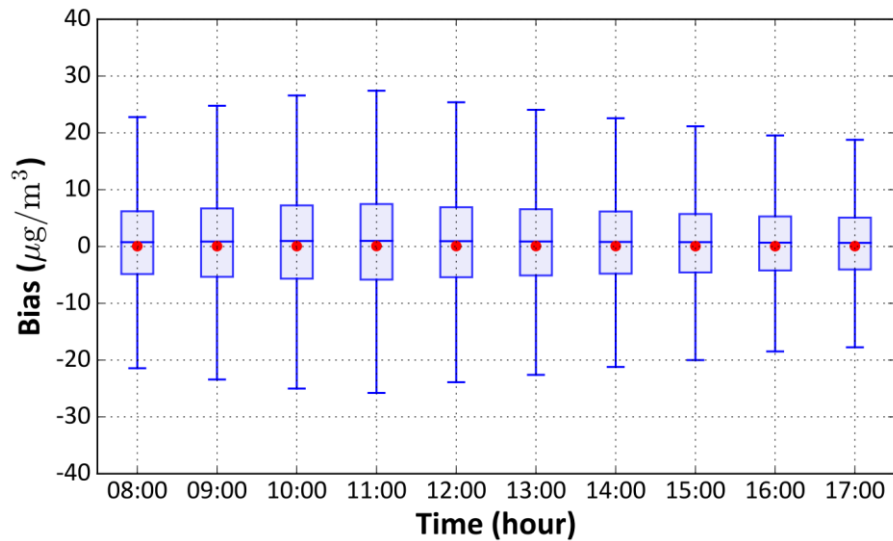


**Figure 6.** Density scatterplots of out-of-sample cross-validation results of hourly PM<sub>2.5</sub> estimates ( $\mu\text{g}/\text{m}^3$ ) in 2018 for (a) eastern China, (b) the Beijing-Tianjin-Hebei (BTH) region, (c) the Yangtze River Delta (YRD), and (d) the Pearl River Delta (PRD) in China.

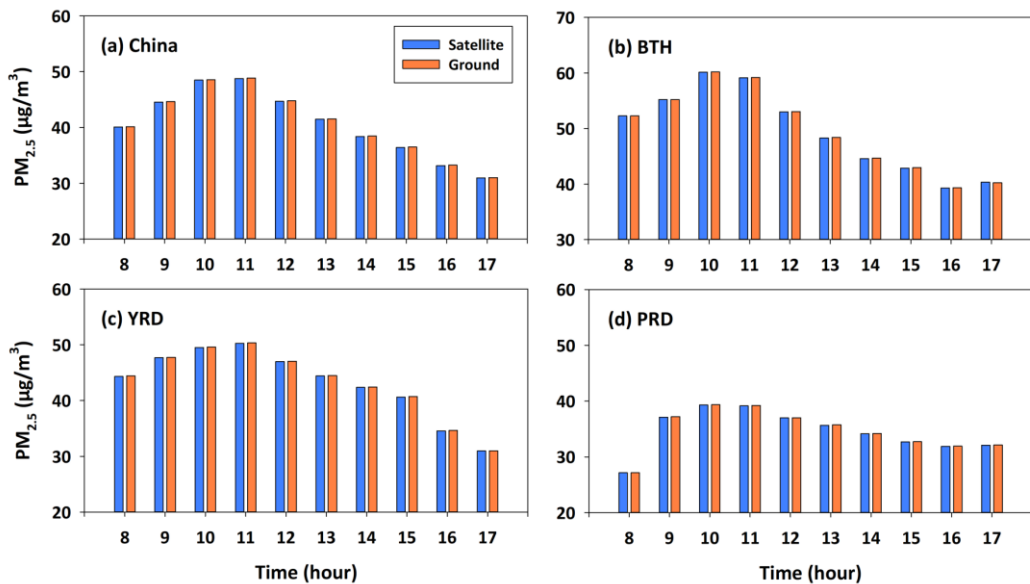


665

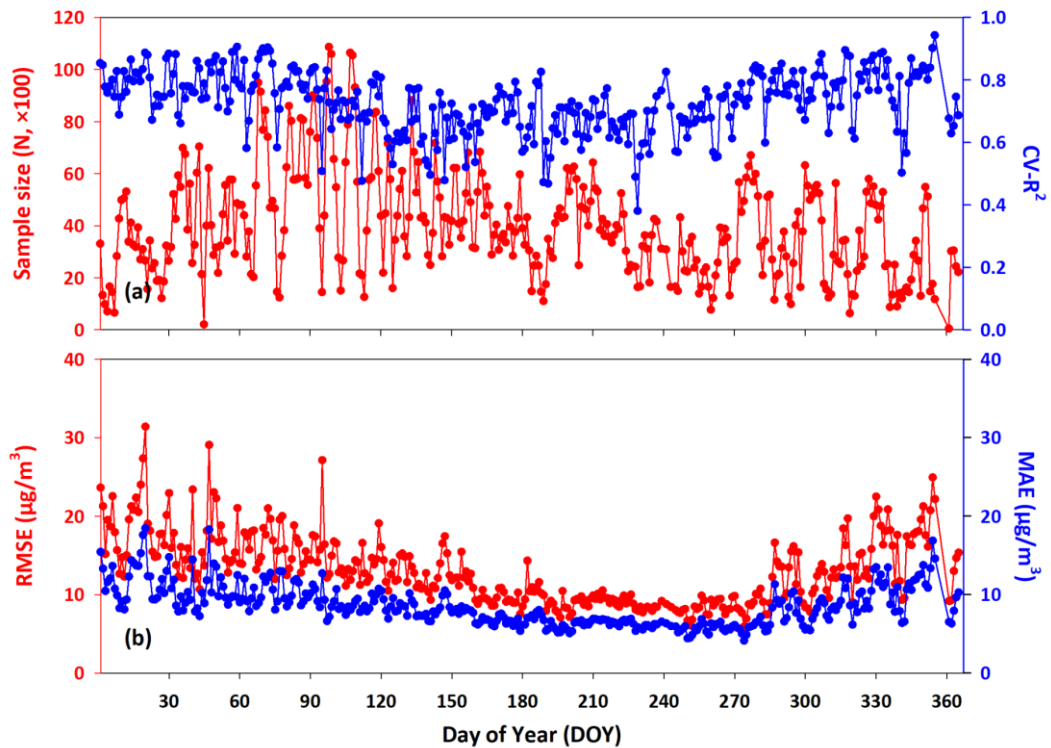
**Figure 7.** Individual-site-scale validation of hourly PM<sub>2.5</sub> estimates ( $\mu\text{g}/\text{m}^3$ ) in 2018 in China in terms of (a) the sample size (N), (b) CV- $R^2$ , (c) RMSE, and (d) MAE.



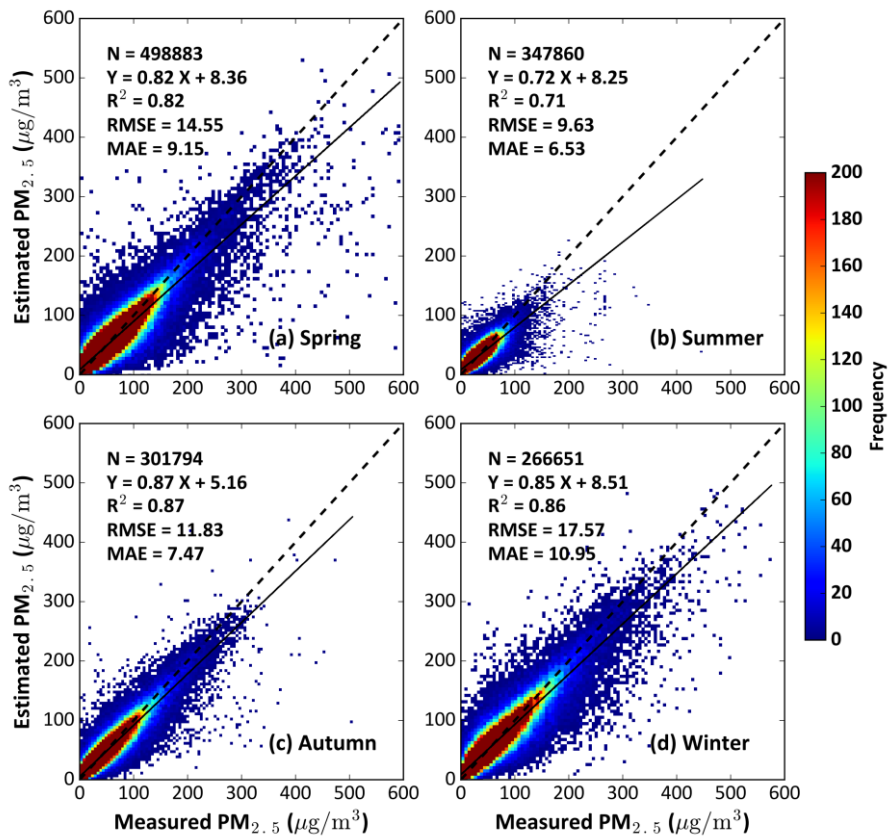
670 **Figure 8.** Boxplots of the temporal dependence of the bias in hourly PM<sub>2.5</sub> estimates ( $\mu\text{g}/\text{m}^3$ ) in 2018 in China. In each box, the red dot represents the mean bias, and the blue middle, lower, and upper horizontal lines represent the median bias, 25<sup>th</sup> percentile, and 75<sup>th</sup> percentile, respectively.



675 **Figure 9.** Time series of Himawari-8-derived (blue bars) and ground-based (orange bars)  $\text{PM}_{2.5}$  diurnal variations ( $\mu\text{g}/\text{m}^3$ ) in (a) China, (b) the Beijing-Tianjin-Hebei (BTH) region, (c) the Yangtze River Delta (YRD), and (d) the Pearl River Delta (PRD).



680 **Figure 10.** Time series of out-of-sample cross-validation of hourly PM<sub>2.5</sub> estimates ( $\mu\text{g}/\text{m}^3$ ) in terms of (a) the sample size (N, red) and  $CV-R^2$  (blue), and (b) RMSE (red) and MAE (blue) in 2018 in China.



685 **Figure 11.** Density scatterplots of out-of-sample cross-validation results of hourly PM<sub>2.5</sub> estimates (μg/m<sup>3</sup>) for (a) spring, (b) summer, (c) autumn, and (d) winter of 2018 in China. Dashed and solid lines denote 1:1 and best-fit lines from linear regression, respectively.

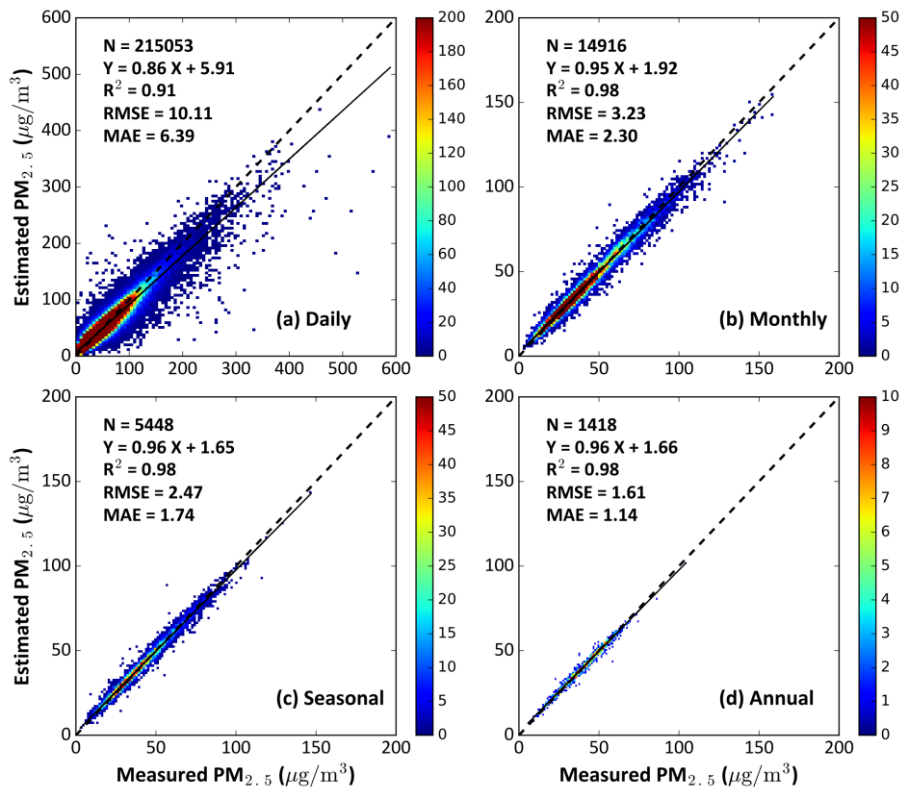


**Figure 12.** Density scatterplots of out-of-sample cross-validation results of (a) daily, (b) monthly, (c) seasonal, and (d) annual mean PM<sub>2.5</sub> estimates (μg/m<sup>3</sup>) in 2018 across China.

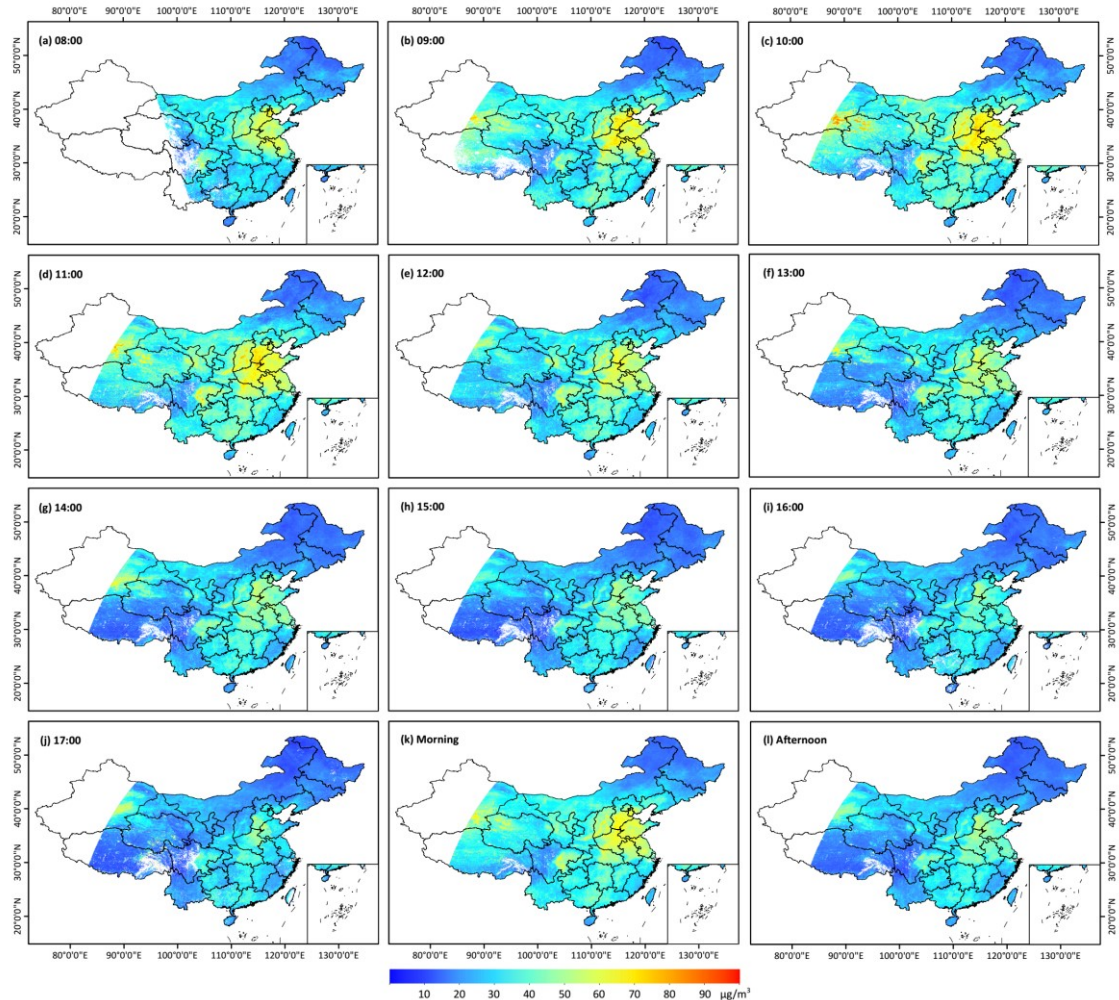
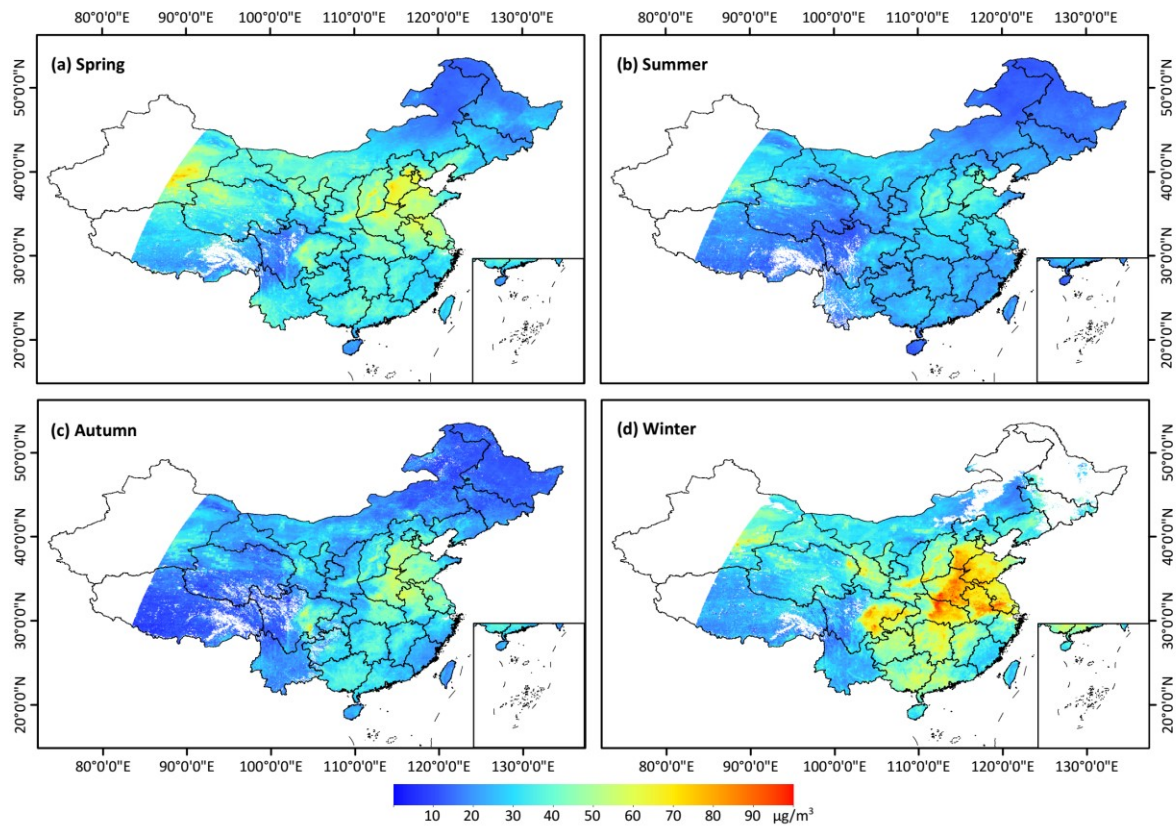
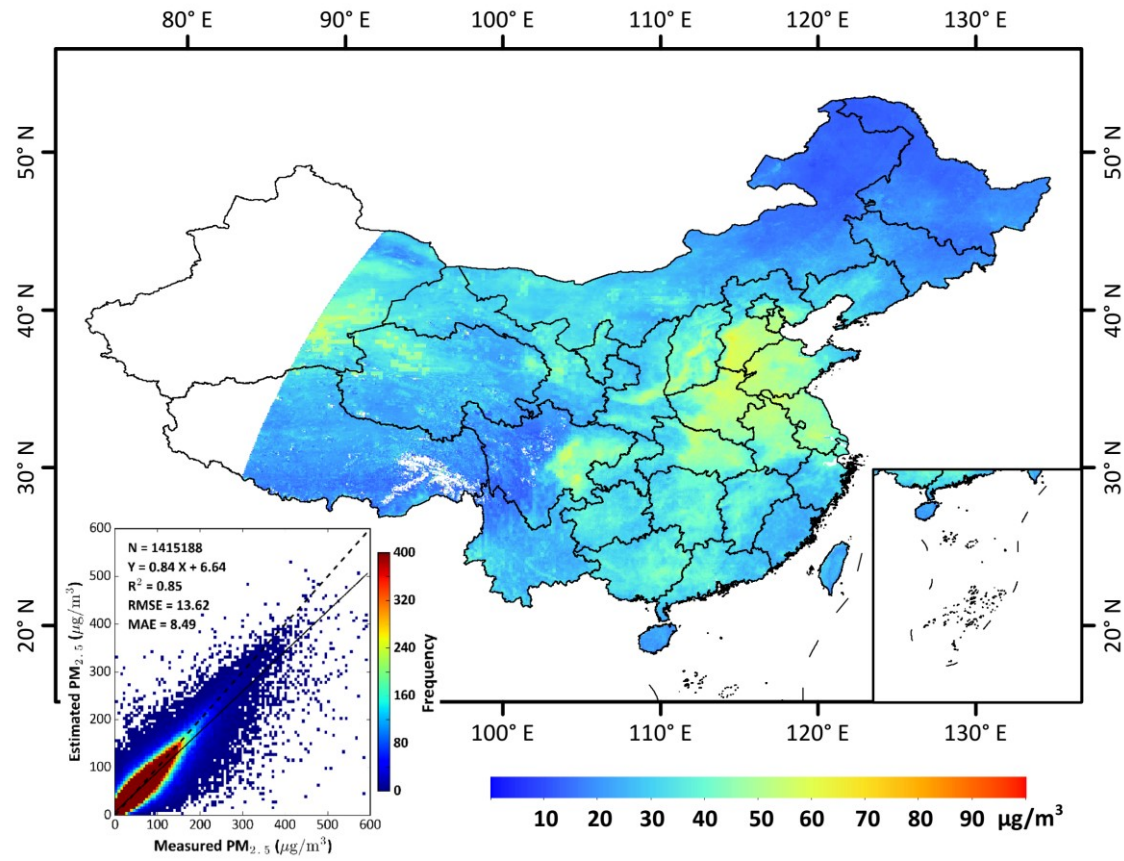


Figure 13. Himawari-8-derived hourly mean PM<sub>2.5</sub> maps (5 km) for different times of the day: (a) 08:00, (b) 09:00, (c) 10:00, (d) 11:00, (e) 12:00, (f) 13:00, (g) 14:00, (h) 15:00, (i) 16:00, (j) 17:00, (k) morning (08:00–12:00), and (l) afternoon (13:00–17:00) local time in 2018 across China.

695



**Figure 14.** Himawari-8-derived seasonal mean PM<sub>2.5</sub> maps (5 km) for (a) spring, (b) summer, (c) autumn, and (d) winter of 2018 across China.



700

**Figure 15.** Himawari-8-derived annual mean PM<sub>2.5</sub> map (5 km) for the year 2018 across China. The lower-left, inserted density scatterplot represents out-of-sample cross-validation results for all hourly PM<sub>2.5</sub> estimates in China.